AIAA SciTech Forum
23-27 January 2023, National Harbor, MD & Online
AIAA SCITECH 2023 Forum

10.2514/6.2023-0823

Test Summary of the Full-Span High-Lift Common Research Model at the ONERA F1 Pressurized Low-Speed Wind Tunnel

Sylvain Mouton[1], Grégoire Charpentier[2]
ONERA, Le Fauga-Mauzac Test Center, 31410 Mauzac, France

Annabelle Lorenski[3]
ONERA, 5 rue des Fortifications, CS 90013, 59045 Lille Cedex, France

The main features and outcomes of the wind tunnel testing of the High-Lift Common Research Model full-span model in the ONERA F1 pressurized low-speed wind tunnel are presented. The test included variation in model configurations, angle of attack, angle of sideslip, Mach and Reynolds numbers, and included force and moment, pressure, wing deformation, and flow visualization data. The main elements of the test methodology are reviewed to better appreciate the quality of the database, in terms of uncertainty, repeatability, and wall and support corrections. A selection of results is presented regarding longitudinal and lateral characteristics, the build-up of the landing configuration, and flap setting effect.

Nomenclature

α	=	Angle of Attack, degrees
β	=	Angle of Sideslip, degrees
b	=	Model half span, $b = 1.50674$ m
C_X	=	Drag coefficient in wind axes
C_Y	=	Side force coefficient in wind axes
C_Z	=	Lift coefficient in wind axes
C_{LAA}	=	Rolling moment coefficient in wind axes
C_{MAA}	=	Pitching moment coefficient in wind axes
C_{NAA}	=	Yawing moment coefficient in wind axes
C_A	=	Axial force coefficient in body axes
C_{YA}	=	Side force coefficient in body axes
C_N	=	Normal force coefficient in body axes
C_{LA}	=	Rolling moment coefficient in body axes
C_{MA}	=	Pitching moment coefficient in body axes
C_{NA}	=	Yawing moment coefficient in body axes
C_p	=	Pressure coefficient
Δ	=	Difference between runs
δz	=	Vertical wing displacement at mid-chord, under wind loading
$\delta\theta$	=	Aerodynamic twist of the wing, under wind loading
M	=	Mach number
Re	=	Reynolds number based on model reference length
p	=	Static pressure
q	=	Dynamic pressure
S_{ref}	=	Model reference surface, $S_{\text{ref}} = 1.00905$ m^2
L_{ref}	=	Model reference length, $L_{\text{ref}} = 0.35925$ m
X, Y, Z	=	Coordinates in tunnel reference frame, with origin at tunnel center
x, y, z	=	Coordinates in model reference frame

Subscripts

0	=	Indicates flow conditions at model location
i	=	Indicates stagnation conditions
c	=	Indicates data fully corrected from wall and support interference

I. Introduction

The continuous rise in computational power in the past decades has prompted the extensive use of Computational Fluid Dynamics (CFD) for the design and analysis of aerospace products. However, the extent to which it can be used to accurately predict aerodynamic characteristics of typical high-lift configurations of transport aircraft remains insufficient to fulfill industrial needs. This originates from limitations in the physical modelling

[1] Assistant Director for Scientific and Technical Development, Le Fauga-Mauzac Wind Tunnel Department.
[2] Test engineer, Le Fauga-Mauzac Wind Tunnel Department.
[3] Model designer, Engineering and Models Department.

and/or numerical discretization of phenomena such as flow separation or boundary transition [1]. Metrics that are important to the success and safety of the aircraft, such as the maximum lift coefficient, are therefore often improperly predicted by simulations, as exemplified in the previous AIAA High-Lift Prediction Workshops (HLPW) [2][3].

As a consequence, the determination of aircraft high-lift performance strongly relies on wind tunnel testing, which also comes with some limitations, such as compromises in the geometrical modeling of the aircraft, or Reynolds number effects.

In order to advance both CFD and wind tunnel capabilities, a High-Lift Common Research Model (CRM-HL) ecosystem has been started to promote dialogue between computational and experimental researchers and practitioners [4]. This ecosystem benefited from a first high-lift configuration [5] based on the high-speed Common Research Model (CRM) shape [6][7]. This configuration was used to manufacture a 10% semi-span model that was first tested at the NASA Langley Research Center 14-by-22 foot atmospheric wind tunnel in late 2018 [8][9], then at the Qinetiq 5 m pressurized wind tunnel in 2019 [10], and again in the 14-by-22 foot tunnel in 2020/2021 for acoustics purpose [11]. Geometry and results from the test in the Qinetiq 5 m tunnel were used in the fourth HLPW (HLPW-4) [3], which also stimulated considerable computational efforts, e.g. [12]. This geometry was however limited by the mechanical capabilities of the 10% semi-span model, so that between 2020 and 2021, some further small improvements were brought to the configuration, to come up with the present "Initial reference configuration" [13], that is intended to be used for the future fifth HLPW (HLPW-5). Based on this shape, a 1/19.5 (≈5.9%) full-span model was designed and manufactured at ONERA, and it was called LRM-HL for "Large Reference Model – High-Lift". This model and test is a follow-up of a broader effort from ONERA to participate in the CRM community, which already produced wind tunnel tests and flow simulations on the high-speed configuration [14][15][16][17]. This effort aims at the following objectives:

- to build an open experimental capability and database for the scientific community,
- to use the models as test benches for the development and demonstration of testing techniques,
- to enable comparisons across wind-tunnels,
- to be a long-term reference model for the wind-tunnels.

In many aspects, these goals were aligned with those exposed in [18] for the purpose of CFD validation, so that recommendations and requirements from [18] could be taken into account.

The present paper introduces the F1 wind tunnel (section II), the LRM-HL model (section III) and the experimental methodologies (section IV). It then presents some results of the test campaign carried out between March 29th and April 19th, 2022 (section V), and presents perspectives for future test campaigns (section VI). However, these results are shown in an unscaled version. As will be detailed in section VII, this was done in the interest of the future fifth HLPW, so that future simulations are carried out "blind", i.e. without any experimental value to adjust to.

II. Overview of the F1 low speed pressurized wind tunnel

Only a brief description of the ONERA F1 wind-tunnel is given here to provide some context of the experimental campaign carried out. The reader is referred to references [19] and [20] for a more complete description. The wind tunnel is of pressurized, closed-circuit type. The rectangular circuit is built of pre-stressed concrete and has an overall volume of some 13 000 m^3. The settling chamber is 12 m in diameter and is fitted with a honeycomb filter and three turbulence screens. It is followed by a metallic convergent which ensures the passage to the rectangular test section, with a 7.2 contraction ratio. The test section is rectangular, 4.5 m wide, 3.5 m high and 11 m long. The side walls are slightly diverging to compensate for the growth of wall boundary layer and achieve negligible stream wise velocity gradient. The wind-tunnel motor is a 9.5 MW asynchronous electric motor, driving a fan of 7.4 m diameter at a constant speed of 360 RPM. The pitch angle of the 16 blades of the fan is controlled to adjust the tunnel speed. A heat exchanger in the return circuit maintains the air temperature in the tunnel to about 25°C to 30°C. To ensure a high productivity, the test section can be isolated from the rest of the circuit by two cylindrical sliding doors, which enables access to the model within 10 min after wind is turned off, while keeping the rest of the circuit pressurized. The test section itself is mounted on a cart that can be removed from the aerodynamic circuit to carry the whole model and testing apparatus from and to different preparation cells in order to optimize the run-up time of the tunnel.

A large number of model setups is available, for full-span models, half-span models, air inlets and propellers, using either internal or floor balance. The wind tunnel is used by worldwide customers to investigate the low-speed aerodynamics of aircraft, but also of air intakes (see e.g. [21]), under high-Reynolds conditions.

The tunnel flow quality was documented with the most recent knowledge in [22]. Across the volume occupied by the full-span models, the dynamic pressure is within ±0.3% and the flow angle within ±0.15° of their mean values. The longitudinal turbulence intensity is lower than 0.08% and the noise intensity is lower than 0.05% (integrated in the 10 Hz – 5 kHz band) over most of the operating envelope of the tunnel (after [19] and more recent unpublished data).

Tunnel calibration procedure to determine flow conditions at model location from tunnel sensors was also explained in details in [22], along with the redundancy checks between the different sensors that are performed for each run.

III. Overview of the LRM-HL wind tunnel model

Figure 1: LRM-HL model on single strut setup in F1 wind tunnel.

A. Model shapes and configurations

As described in section I, the LRM-HL is a 1/19.5 (≈5.9%) scale full-span model of the "Initial reference configuration" of the CRM-HL [13]. The model span is 3.02155 m and the fuselage length is 3.30063 m. All dimensions in this paper are provided at model scale.

1. Clean wing LRM

This paper is mostly about the test of the high-lift model, however some results from the clean wing model will also be presented. The shape of the clean wing LRM corresponds to the high-speed wing shape of the CRM, as described in [7]. As explained in [5], this clean wing geometry is not fully identical to the CRM-HL wing with stowed high-lift devices. Most notably the high-lift wing has a larger leading edge radius on the slat, a constant dihedral angle and a different trailing edge thickness.

2. High-Lift LRM

This model shares the same fuselage and empennages than the clean wing model. The shapes, and especially the high-lift system and nacelles, have been described in [13]. CAD model of the wing have been shared within the CRM-HL ecosystem, and integrated into the design. However, this CAD model did not specify shape for the slat brackets, the flap brackets and the Flap Track Fairings (FTFs), only their number and spanwise position was available, completed by guidelines for their size and architecture given in [13]. Therefore, slat and flap brackets were designed for the present model, incorporating these pieces of information. The FTFs from HLPW-4 geometry were reused, only slightly adapted to cope with their new position. They were also broken down into an underwing fixed part and a moveable part, connected with a hinge line. Due to schedule issue, the final release of the Wing Under Slat Surface (WUSS) of the CRM-HL reference configuration could not be used for that model. This resulted in local deviation (0.6 mm), but only on the most outboard part of the wing. 2D simulations tend to indicate that this small deviation is expected not to change the flow physics or wing performance.

The high-lift devices can be set in take-off reference configuration (T/O) or landing reference configuration (LDG). Alternate landing configuration (LDG−3 and LDG+3) are also available, see Table 1. It is also possible to

stow the flap into the wing to retrieve the shape of the trailing edge of the clean wing (STOWED). The nacelles can be removed from the model, and a filler piece is then fitted to ensure continuity of the slat through the whole span, as was already done in [8].

Table 1: Slat and flap settings.

Configuration	Slat deflection (inboard / outboard)	Flap deflection (inboard / outboard)
T/O	22° / 22°	25° / 25°
LDG	30° / 30°	40°/37°
LDG−3	30° / 30°	37°/34°
LDG+3	30° / 30°	43°/40°
STOWED	30° / 30°	0° / 0° (stowed)

B. Model design and manufacture

The model was produced by the ONERA model design and manufacturing department located in Lille. It was meant to be as accurate as possible. For example, the pressure tubes connected to pressure taps on the slats are routed inside the slat brackets, without any aerodynamic obstruction in the slat gap.

A geometrical inspection was performed on the model, with the help of a mobile 3D measuring arm (Faro® Quantum measurement system). 15 sections were checked on each of the high-lift wings, and all of the 5 wing configurations described in Table 1 were inspected. Deviations resulting from this inspection are listed in the Table 2. From these results, the model is considered highly accurate. For example, the maximum positioning error of slats and flaps, that has a direct effect on the gaps between the high-lift elements, is within 0.295 mm/236 mm = 0.13% of the wing mean aerodynamic chord.

Table 2: Main results from geometrical inspection of the model (first value reported is the maximum measured across all inspected sections and all wing configurations; second value, written pω, indicates the ω^{th} percentile).

		Wing main body	Slats	Flaps	HTP	VTP	Fuselage
Positioning error	Twist	0.062° p85: 0.017°	0.220°	0.060°	0.014°	0.006°	N/A
	Dihedral	0.023°	N/A	N/A	0.017°	0.005°	N/A
	Sweep	0.012°	N/A	N/A	0.006°	0.017°	N/A
	Translation w.r.t. wing main body	N/A	0.267 mm p97: 0.15mm	0.295 mm p85: 0.15 mm	N/A	N/A	N/A
Shape error	position < 10% chord	0.066 mm	0.108 mm p71: 0.075 mm	0.069 mm p95: 0.05 mm	0.062 mm	0.031 mm	0.255 mm p89: 0.15 mm
	position > 10% chord	0.146 mm p94: 0.05 mm					
Roughness arithmetic average Ra			0.31 µm		0.38µm	0.32µm	0.48µm

C. Model setup in the wind tunnel

For the test reported here, the LRM-HL model was mounted on the single-strut setup, using a 6-component internal balance. The pitch movement is achieved by a carriage travelling on a cradle under the floor, so that the model rotates approximately around the tunnel center. The maximum range of pitch angle for this test was about −10° to +24°. Movement in azimuth is achieved thanks to a turntable also located under the floor, and the range of azimuth angle was ±30°.

D. Model finish

Once assembled during the test preparation, the model surface is prepared for the aerodynamic test. This consists in ensuring proper sealing between model parts in spite of the inevitable assembly game, filling or taping the holes housing assembly screws and pins, cleaning up the model surface and applying the device tripping the transition of the boundary layer. The result of these operations is presented as pictures in Figure 2.

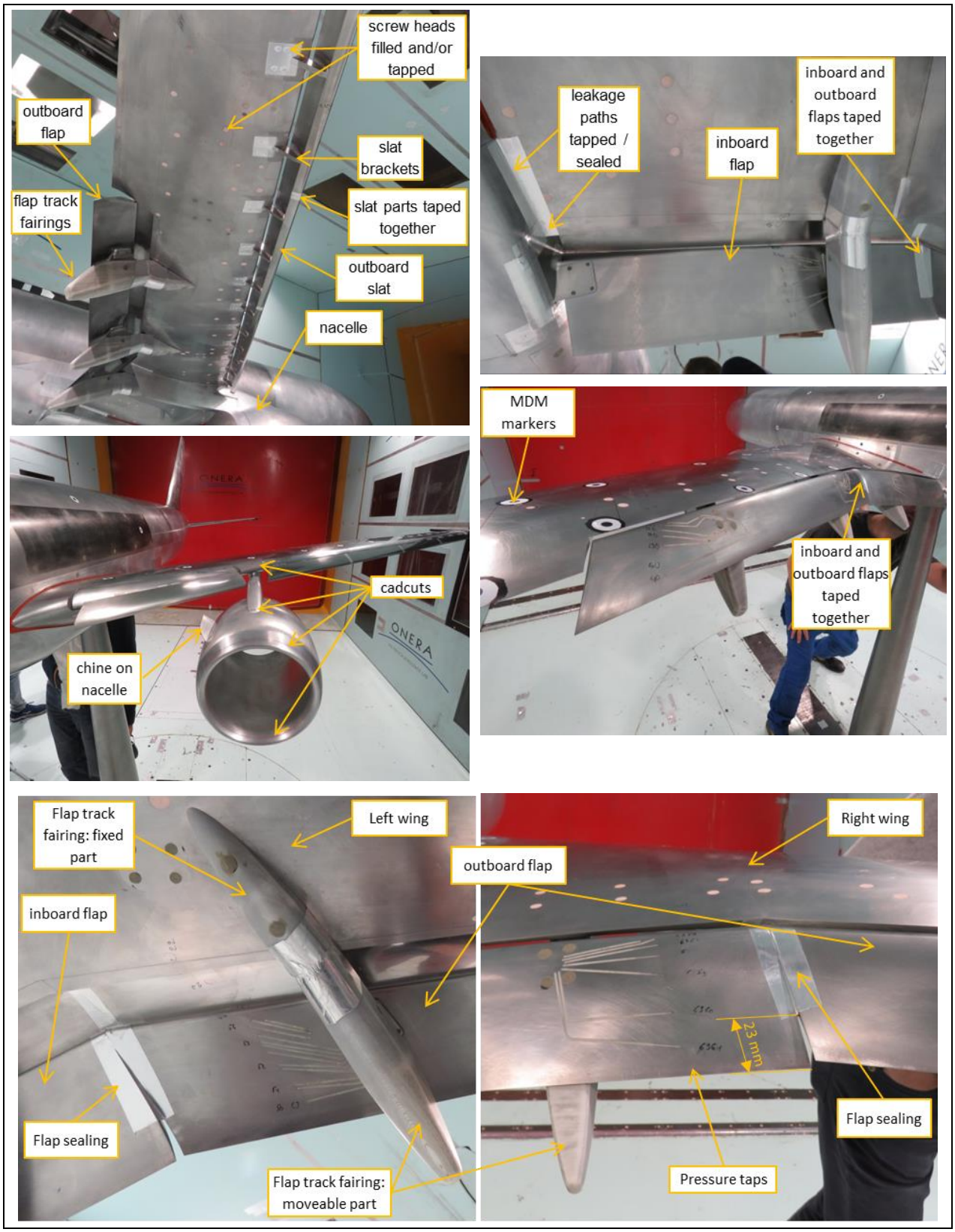

Figure 2: Details of the wind tunnel model in LDG configuration.

The boundary layer transition was tripped using so-called "cadcut" strips. Each strip is glued on the model surface and consists in a row of circular dots of 1.27 mm diameter, placed every 2.54 mm. The thickness of the dots for this test was 114 µm on the empennages, and 127 µm on the fuselage, wings and nacelles. This thickness was selected in order to be comparable to the test in Qinetiq 5 m wind tunnel [3], once the difference in model scale is taken into account. The location of the transition trips is indicated in Figure 3, with all dimensions given at model scale. No tripping is applied on section of the wings where slats and flaps are present.

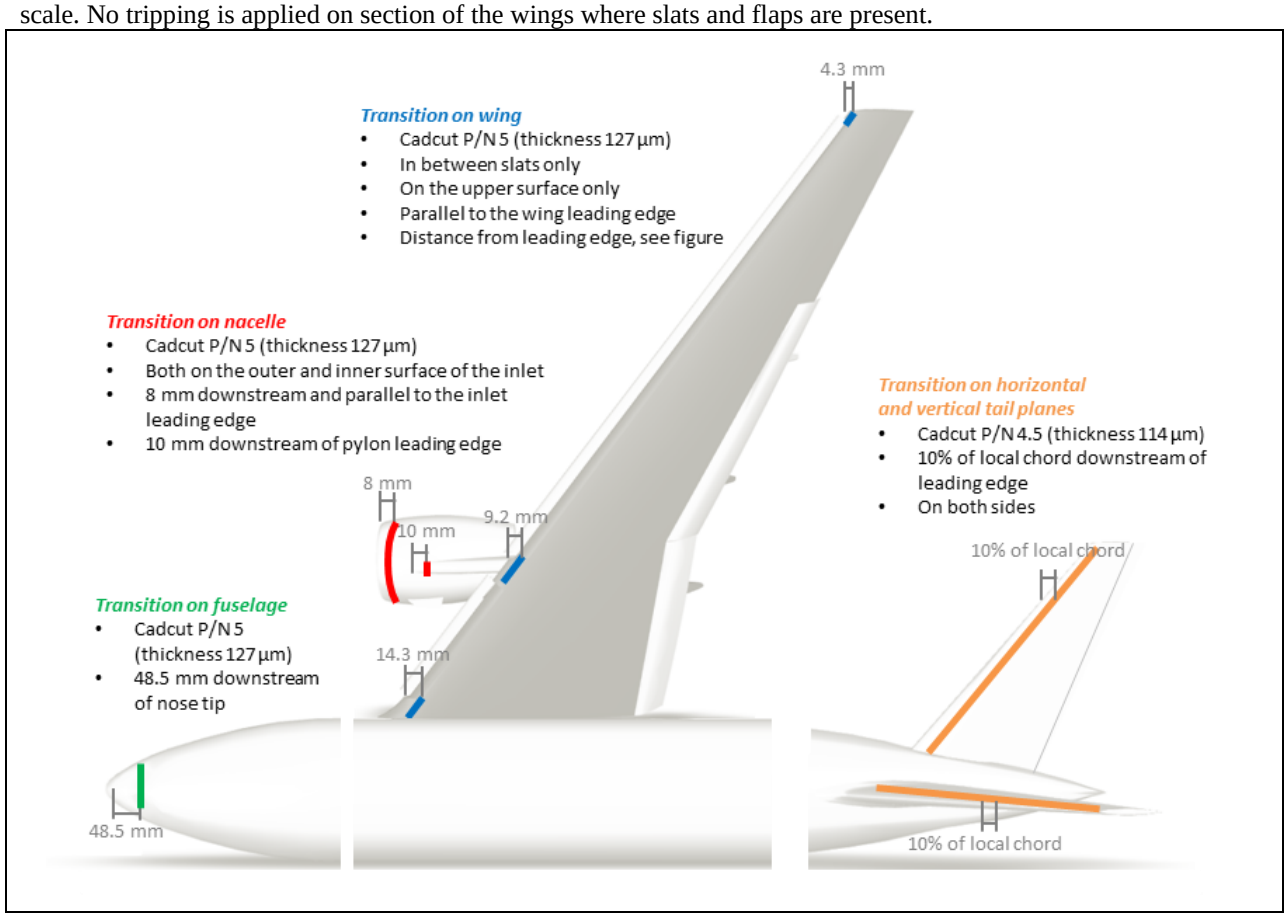

Figure 3: Details of the boundary layer transition.

IV. Test methodology

This section is illustrated with experimental results that were all obtained on the LDG conf, with tail planes, at a Mach number M_{0c} = 0.20 and a Reynolds number Re_{0c} = 5.9 million.

A. Sensors in the experiment

The main sensors involved in the experiment are presented in Table 3. The first part of the table lists the usual wind tunnel reference sensors that are used to determine the flow conditions in the test section. Using tunnel calibration laws, these reference sensors allow determining the flow conditions at model location in the wind tunnel, more especially total pressure, total temperature, and static pressure [22]. The second part of the table lists the main sensors dedicated to the present model and experiment. Some additional unlisted sensors are used to ensure in-situ calibration and monitoring of the pressure scanners. There also exist numerous sensors dedicated to the monitoring of the tunnel operation, but that are not used in the processing of the data reported in this paper.

Table 3: List of sensors in the experiment.

Sensor	number and location	Quantity measured
Differential pressure sensor	6 behind wind tunnel walls (2.5 psi range)	Difference between reference total pressures and reference static pressures
Differential pressure sensor	2 behind wind tunnel walls (50 psi range)	Difference between reference total pressures and atmospheric pressure
Thermocouple	1 in settling chamber (type K)	Total temperature
Barometer	1 in instrumentation room	Local atmospheric pressure
Humidity sensor	1 in tunnel circuit	Moisture content of the air in the tunnel
Force balance PHI180 N°3	1 inside the model fuselage	the 6 components of the force acting on the model
Inclinometers	2 inside the model fuselage	pitch angle of the model
Angular potentiometer	1 under the floor	azimuth angle of the model
Electrical level	1 inside the model fuselage	horizontality of the model
Spirit level	1 on top of model fuselage	horizontality of the model
Differential Electronic Pressure Scanners (ESP)	8 inside the model fuselage (15 psi range) 3 under the floor (5 psi range)	static pressure on model surface static pressure on wind tunnel walls
PSI®	PSI® 8400 system in instrumentation bay	
Strain gauges	3 half bridges in the right wing	Bending moment in the wing
Accelerometers	8 inside the model fuselage and wings	Model accelerations
Contact detection	1 between strut and model	Absence of contact between metric and non-metric parts
Cameras for Model Deformation Measurement	2 behind windows on the ceiling	Pictures of wing markers

449 static pressure measurements are distributed over the model and 115 on the wind-tunnel walls, as indicated in Table 4.

Table 4: Static pressure taps on the model and wind-tunnel walls.

Part	Number of taps	Comments
Fuselage	48	including 12 near the strut
Vertical tail plane	27	over 1 section
Horizontal tail plane	81	over 3 sections, 2 on the left, 1 on the right
Wing	289	over 7 sections 3 on the left, 4 on the right, typically with 10 taps on the slat, 18 to 25 on the main body and 12 to 16 on the flap
Nacelle	4	Inside the right nacelle
Tunnel ceiling	45	over 3 rows
Tunnel left wall	35	over 3 rows
Tunnel right wall	35	over 3 rows
Total	564	

B. Measurement uncertainty

A detailed discussion on uncertainty is not the purpose of this paper. This section will therefore only provide the driving causes and the order of magnitude of the uncertainty in the present test. Uncertainty is regarded as Gaussian and is here provided as two sigma (95%) confidence intervals.

1. Uncertainty on forces

The uncertainty of balance reading is estimated to be 10^{-3} of its measurement capacity on each component. This yields the Table 5 for the contribution of the balance to uncertainty on aerodynamic coefficients in body axes.

Table 5: Balance capacity and 2-σ uncertainty on force coefficients at 10 kPa dynamic pressure.

Component	Axial force	Side force	Normal force	Rolling moment	Pitching moment	Yawing moment
Measurement capacity	±8310 N	±29 540 N	±92 210 N	±10 240 Nm	±15 140 Nm	±3 920 Nm
Uncertainty on aero. coef	$\pm 8\times10^{-4}$	$\pm 3\times10^{-3}$	$\pm 9\times10^{-3}$	$\pm 3\times10^{-3}$	$\pm 4\times10^{-3}$	$\pm 1\times10^{-3}$

2. Uncertainty on dynamic pressure

The key measurement to determine the dynamic pressure q_0, and therefore a key contributor to its uncertainty, is the measurement of differential pressure $p_{i0} - p_0$ between total and static pressure. As explained in [22], this is not directly measurable during the test. Instead, the differential pressure between a reference total pressure in the settling chamber and a reference static pressure near the entry of the test section is measured instead. Calibration laws, determined during empty tunnel calibration, are then used in order to deduce p_{i0}, $p_{i0} - p_0$, and finally q_0 in the test section. Actually, this differential pressure measurement is carried out by 6 redundant sensors (of 3 different types) of 2.5 psi capacity, independently connected to 6 different static pressure taps and 3 total pressure taps. In the present test, the sensor connected to the reference tap "C18" was used as the primary source of data. This gives the opportunity to compare each of the 5 other measurements, to experimentally evaluate the uncertainty on $p_{i0} - p_0$, which is itself almost equal to the uncertainty on dynamic pressure q_0. Examination of Figure 4 reveals that this uncertainty if of the order of 35 Pa (two sigma value) at the highest dynamic pressure, and reduces to 15 Pa at the lower end of dynamic pressure range, which allows to derive Table 6. These observed values are consistent with the statements in the datasheets of the sensors and measurement hardware. The corresponding uncertainty on velocity, Mach number and Reynolds number is negligible for subsonic testing.

Table 6: 2-σ uncertainty on dynamic pressure.

Dynamic pressure	q_0 = 2 kPa	q_0 = 14 kPa
Uncertainty on dynamic pressure	±15 Pa	±35 Pa
Relative uncertainty on dynamic pressure	±0.75%	±0.25%

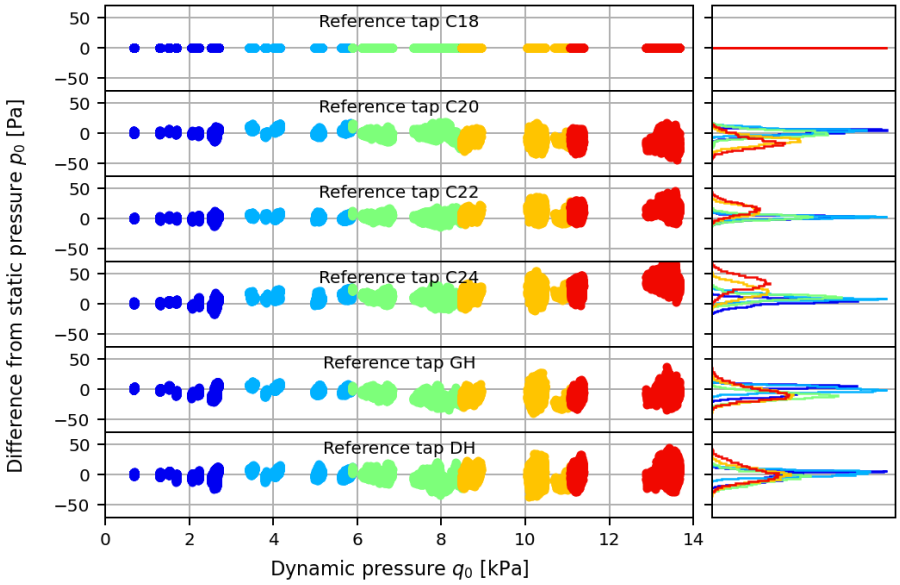

Figure 4: Comparison of readings from redundant sensors for the determination of tunnel static pressure p_0 (all runs of test campaign, tap C18 used as reference; points are grouped into 5 ranges of dynamic pressure, corresponding to the 5 colors, to plot histograms on the right).

3. Uncertainty on angle of attack

Limiting ourselves to zero-sideslip runs, the Angle of Attack (AoA) is the sum of model pitch angle and tunnel upwash. From sensor datasheet, the uncertainty on model pitch angle measurement is below 0.01°, and it can be confirmed by comparing the two redundant sensors placed in the model. The uncertainty on tunnel upwash is

estimated to be ±0.02° [22]. Total uncertainty is then about 0.024°. It is worth noting that the pitch angle error is random across runs, whereas the tunnel upwash error is constant, and therefore does not intervene when comparing different runs.

4. Example of combined uncertainty on lift, drag and pitching moment

Uncertainty on force coefficients can be obtained by propagating the above sources into the calculations, assuming statistically independent errors. An example of typical result is provided in Table 7 for a case at Mach 0.20 and a total pressure of 3.82 bar, which yields a dynamic pressure of 10 kPa and a Reynolds number of 5.9 million.

Table 7: Example of typical 2-σ uncertainty on longitudinal force coefficients for a dynamic pressure of 10 kPa.

Parameter	Value	Uncertainty	Relative uncertainty
AoA	15°	±0.024°	±0.2%
Lift	2	±0.011	±0.6%
Drag	0.20	±0.0027	±1.4%
Pitching moment	−0.30	±0.0043	±1.4%

5. Uncertainty on model pressure coefficients

The uncertainty on model pressure coefficient $C_p = (p - p_0)/q_0$ originates from the measurement of the differential pressure $p - p_0$ on one side, that implies the Electronic Pressure Scanners (ESP) plus another differential pressure sensor; and the measurement of the dynamic pressure q_0 on the other side (see IV.B.2). As a result, the uncertainty is dependent on the flow conditions. Some examples are provided in the Table 8.

Table 8: 2-σ uncertainty on pressure coefficient.

Pressure coefficient	q_0 = 2 kPa	q_0 = 14 kPa
$C_p = 0$	±0.08	±0.01
$C_p = -10$	±0.11	±0.03

C. Continuous polars

During tests in F1, most of the runs are performed by continuously varying one of the test parameter and taking properly filtered and synchronized samples from the acquisition systems. In the present case, the AoA was varied at a rate of 0.3 degree/second (pitch-sweep run a.k.a. AoA-sweep run), and the Angle of Sideslip (AoS) at a rate of 0.5 degree/second (AoS-sweep run). Data stream for the forces and angles measurements is numerically filtered by a low-pass filter with a cutoff frequency of 1 Hz, and finally sampled at a rate of 2 points/second. With this setting, a pitch-sweep run with corrected AoA rising from about −9° to +23° is carried out in about 1 min 45 s and includes about 210 data points, one every 0.15°. Model pressure measurements are performed using a PSI® 8400 system, that scans the 10×64 different pressure ports at about 20 kHz, and returns the average of 6 samples, also at a rate of 2 points/second. The pneumatic tubing in between the pressure orifice and the sensor contributes to filter out the high frequency pressure fluctuations. Model deformation measurements are performed by cameras at rate of 1 point/second, unfiltered. The delays introduced by the different measurement systems are accounted for, so that data points are properly synchronized.

Figure 5 shows a comparison of data obtained during a continuous pitch-sweep run and data acquired under the same conditions but with a non-moving model (pitch-pause runs). Pitch-pause runs were carried out with the same acquisition rate and characteristics, over a duration of 60 s, i.e. 120 samples. All samples are shown in Figure 5 even if they visually collapse to single points, except past stall (in purple), which shows the scatter due to flow unsteadiness and model movements. The Figure 6 displays the same data plotted as differences in force coefficients between pitch-sweep and pitch-pause runs. These differences are mostly below 0.01 in lift, 10×10^{-4} in drag and 5×10^{-3} in pitching moment coefficients, which is less than the uncertainty exposed in IV.B. Only past stall does the scatter considerably increase, as previously mentioned, but the average of the samples stays within the limits of the plot, with a difference in averaged lift coefficient of only 0.03 between pitch-sweep and pitch-pause runs. These results demonstrate that data filtering performed during continuous pitch-sweep runs was adequate to reject the high-frequency content in the signal, mostly introduced by the model and strut moving around their first eigenmode around 5 Hz, and to preserve only the quasi-steady aerodynamic forces in the low frequency range.

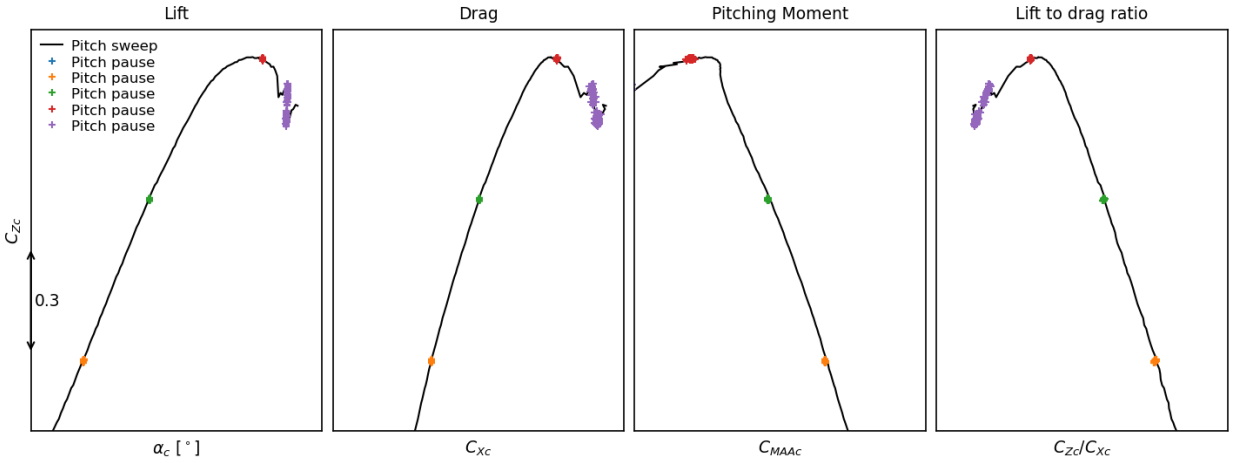

Figure 5: Comparison of force coefficients obtained during pitch-sweep and pitch-pause acquisition (runs 1387, 1407, 1408, 1409, 1410, 1411).

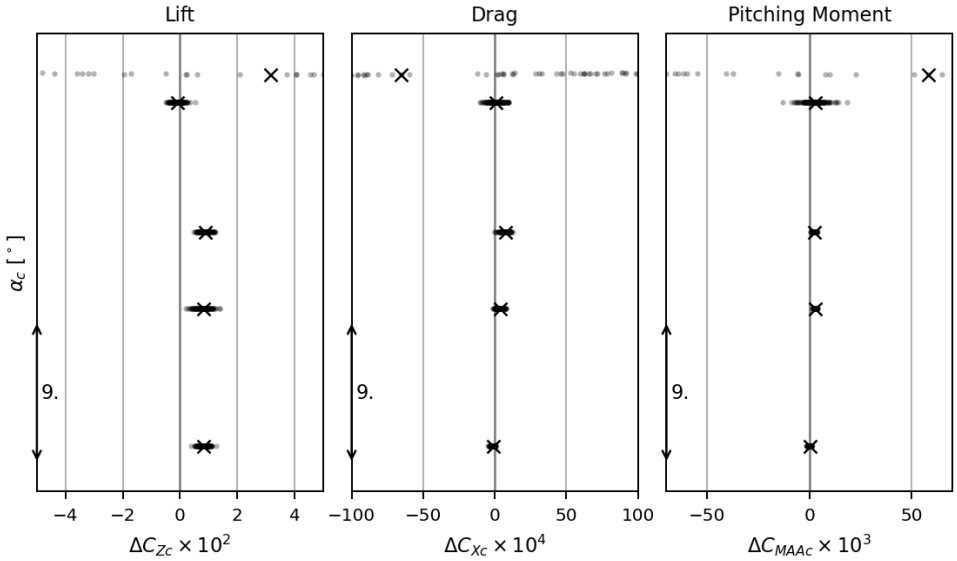

Figure 6: Difference in force coefficients between pitch-pause and pitch-sweep acquisition; each grey dot is a pitch-pause data point, and their average is shown as a cross (runs 1387, 1407, 1408, 1409, 1410, 1411).

To prove the good synchronization between the pressure measurements carried out with ESP and the rest of the data, we now examine the difference in pressure coefficient measured between one of the pitch-pause runs (the one near maximum lift, in red in Figure 5) and the same data measured during pitch-sweep runs. During these runs, there were 432 pressure taps out of 449 active on the model (96.2%), because the remaining taps had been detected as leaking or clamped during pre-run check. Hence the comparison between pitch-sweep and pitch-pause runs results in 432 differences in pressure coefficient, which are presented as a histogram in Figure 7.

It can be observed that the difference is within ±0.02 for 95% the taps, which is in agreement with the uncertainty exposed in section IV.B. Only 9 outliers exhibited $|\Delta C_p| > 0.05$. Further examination revealed that these outliers are located in regions strongly influenced by separated or vortical flow (e.g. downstream of the nacelle) that exhibit strong pressure fluctuations that were not completely eliminated by the pneumatic and electronic filtering during the pitch-sweep runs.

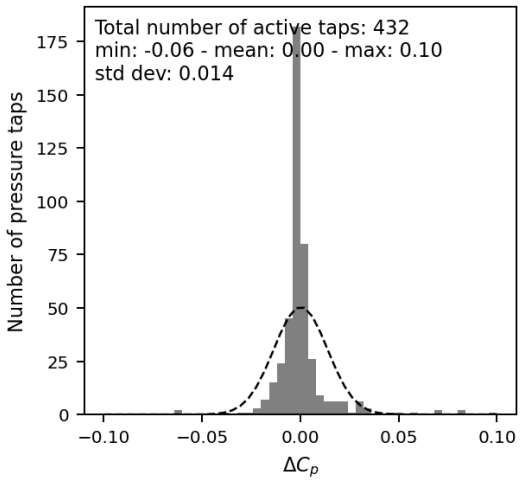

Figure 7: Histogram of differences in pressure coefficients between pitch-sweep (run 1387) and pitch-pause (run 1410) acquisition, near maximum lift. The dashed line is a Gaussian distribution having the same mean and standard deviation.

D. Repeatability

In F1 wind-tunnel, the short-term repeatability is always verified by performing a down-sweep polar immediately after each up-sweep polar. This allows immediately identifying any drift or hysteresis in the measurement process, but also sometimes small model deterioration, such as a piece of adhesive tape being peeled off the surface. The result of this comparison is shown in Figure 8, for a run in LDG configuration, at Mach 0.20 and a Reynolds number of 5.9 million. At this plot scale, the only difference that can be spotted is a classical hysteresis effect past stall. Interestingly, this configuration presents with a limited amount of hysteresis that manifests itself only about 2° beyond maximum lift. Figure 9 shows the same data presented as differences between up- and down-sweep runs. The magnitude of these differences is comparable to the scatter observed in Figure 6 and representative of the uncertainty exposed in section IV.B. The larger difference at high AoA, past maximum lift, is related to the hysteresis effect, mentioned above.

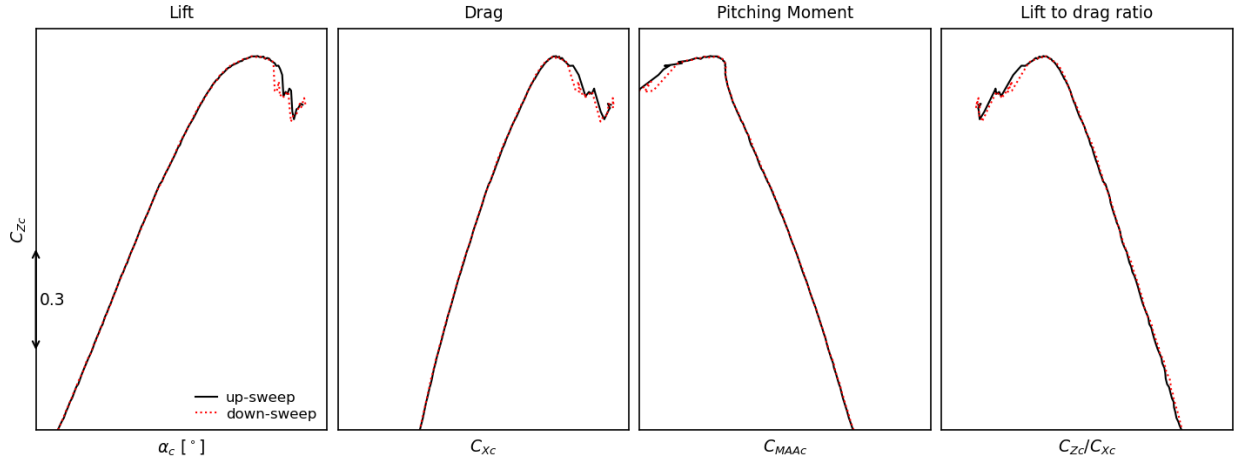

Figure 8: Force coefficients measured during up-sweep (run 1387) and a down-sweep (run 1388) runs.

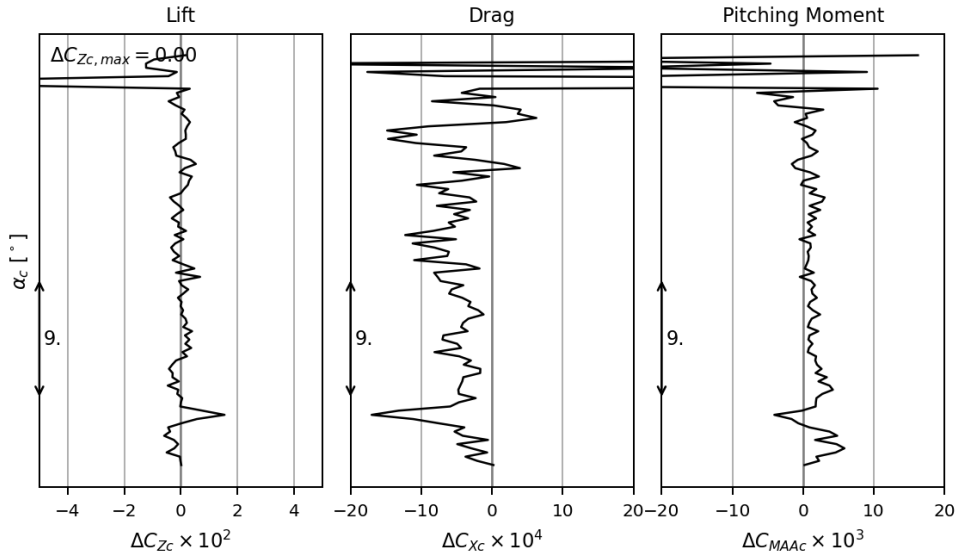

Figure 9: Difference in force coefficients between up-sweep (run 1387) and a down-sweep (run 1388) runs.

More interesting is the mid-term repeatability shown in Figure 10, which compares force coefficients from run 1387 and 1788. In between these two runs, 14 tunnel rotations have elapsed, the tufts have been set and removed on the right wing, oil flow visualization has been performed twice on the right wing, the nacelles were removed and put back again, and the flaps have been stowed (for the component build-up investigation reported in section V.D), then set back into LDG configuration, which implied reapplying the sealing and tape on all the flaps and flap track fairings. The repeatability was almost as good as in the short-term, below 0.015 in lift, 15×10^{-4} in drag and 5×10^{-3} in pitching moment coefficients, very much representative of the uncertainty values exposed in section IV.B.

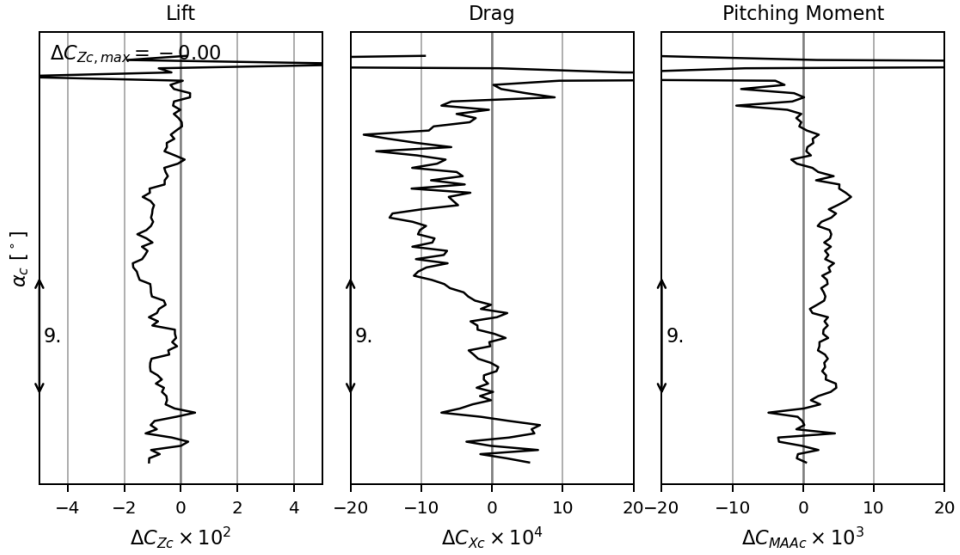

Figure 10: Difference in force coefficients between runs at the beginning (run 1387) and at the end (run 1788) of the test campaign.

In between 1387 & 1788, some other repeats were regularly performed (runs 1594, 1614, 1617 and 1659). They sometimes showed less lift (−0.01 to −0.04 for a given AoA) and more nose down moment (−0.010 to −0.020 for a given lift coefficient) at $\alpha_c \lesssim 15°$, see Figure 11. After examination of lateral forces and pressure measurements, this could be traced to a physical phenomenon occurring on the inner right flap that caused the inboard right wing sections to produce slightly less lift than the left sections. Although this phenomenon was measurable, its magnitude was deemed sufficiently small not to deserve further investigation, but it points out that the flow on the inner flap at

low AoA is very sensitive to small details of the configuration. At higher AoAs $\alpha_c \gtrsim 15°$, repeatability was very good throughout the whole campaign, and the maximum lift coefficient was repeated to better than 0.005 for the LDG configuration, at Mach 0.20 and a Reynolds number of 5.9 million.

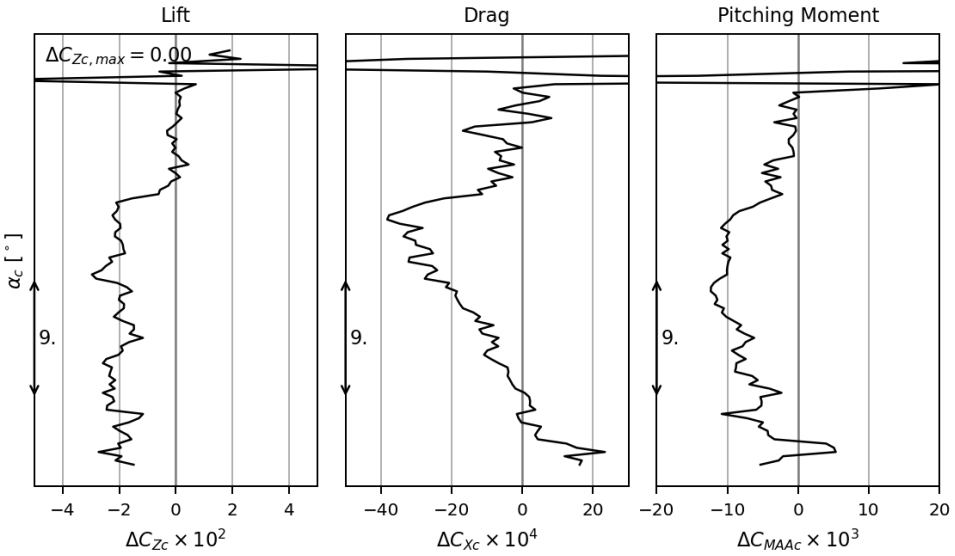

Figure 11: Difference in force coefficients between run 1387 and run 1659.

E. Wall corrections

In ONERA wind tunnels, the modeling of wall interference is based on linearized potential theory [23]. The aircraft model is represented by a set of point singularities, distributed over the fuselage, wing and horizontal tail plane. The position and intensity of each singularity is computed based on geometrical properties of the model (e.g. local chord, local cross-section), but also on actual measurements (lift and drag). In the case of F1, the boundary condition imposed by the solid rectangular walls could easily be solved by the method of images, but in fact the software uses Fourier transforms in order to be also able to cope with the porous walls encountered in transonic wind-tunnels. This modeling can output the complete three-dimensional wall-induced interference flow-field. This flow-field is then space-averaged along the span of the wing and empennage to come up with corrections in flow velocity and angle (known as first-order corrections [24] or primary corrections [25]). The spatial variation in the wall-induced flow-field is then taken into account with complementary corrections of axial force and pitching moment angle (known as second-order corrections [24] or residual variations [25]).

The validity of this set of corrections has been verified over the years by comparing results across wind tunnels (e.g. [26], [27]), with flight tests (e.g. [28]), and more recently with more advanced flow modelling (e.g. [24]). Additionally, it is possible to compare the pressure on the wind-tunnel walls predicted by the linearized potential model, with the pressure actually measured during the test. This is the purpose of the Figure 12. To obtain this figure, pressure coefficients measured during the empty tunnel calibration $C_{p,\text{empty}}$ were subtracted from the pressure coefficients of the present campaign C_p, as recommended in [25], §8.3.2. Because the flow potential model is used to derive wall corrections only, it usually does not include the single-strut support. The effect of the support is accounted for in the support corrections described in the next section. However, to produce the plot of Figure 12, a flow potential model of the support was included in the modeling, mostly to represent the blockage effect of the support wake. The area without measurements for $-1 \text{ m} < X < 2 \text{ m}$ originates from the large glass windows installed on the tunnel side walls and visible in Figure 1. As mentioned in [25], the signal to measure is small and it is difficult to maintain high quality pressure tap orifices on the walls of a large wind tunnel, so that a couple of taps exhibit small inconsistencies (±0.015 in pressure coefficient). However, the overall agreement with the flow potential model is good. It validates the wall correction method by showing that the model description by means of discrete singularities is successful, and that, therefore, the wall-induced interference flow-field is also properly simulated.

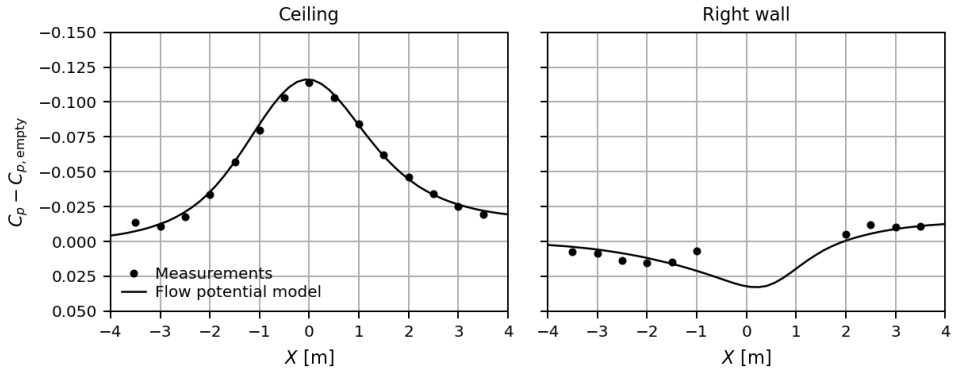

Figure 12: Pressure coefficient on wind tunnel walls, at maximum lift coefficient (run 1387).

F. Support corrections

The support corrections for this experimental setup were derived from a previous wind tunnel test involving the clean wing version of the LRM model, which shares the same fuselage and support systems. During this experiment, a dummy strut was attached to the non-metric part of the setup, see Figure 13. This dummy strut was then removed to observe the effect on force coefficients. Like in the case of wall corrections exposed above, this effect was broken down between first-order corrections on flow velocity and angle, that are independent of the aircraft configuration and explain a large part of the support effect, and second-order corrections on axial force and pitching moment. Previous experience [29] indicates that this second-order correction mostly impacts the fuselage and tail plane so that results obtained on the clean wing configuration may be used to process the high-lift configuration as well.

All results presented in this paper are all fully corrected for wall and support interference, as indicated by the subscript “c” on each quantity reported.

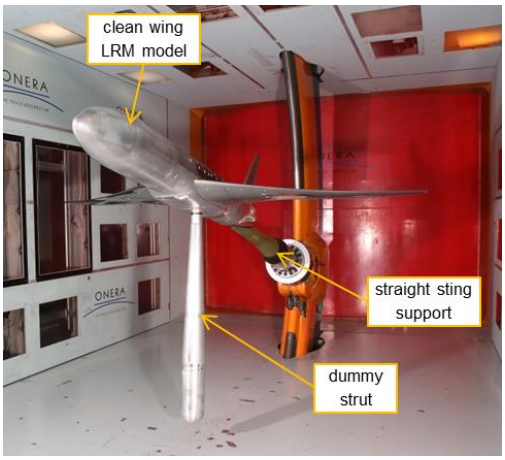

Figure 13: Experimental setup for the single strut effect test.

G. Oil flow visualization

Some oil flow visualizations were carried out on the right wing during the test campaign. The model was painted with a mixture of mineral oil and colored pigments, using different colors on different parts of the wing. The model is then exposed to the air flow at desired conditions for a few minutes. Photographs are taken during and after the run under UV illumination.

H. Model deformation measurement

Wing deformation was measured during most of the test campaign. Stereovision technique described in [32] was used for that purpose, using the markers visible in Figure 2.

V. Overview of aerodynamic results

A. Landing configuration, with tail planes

1. *Longitudinal characteristics*

The Figure 14 shows longitudinal force coefficients of the LDG configuration, at a Mach number of 0.20 and for increasing Reynolds number from 1.6 to 5.9 million, corresponding to the wind tunnel test envelope when pressurized from 1 to 3.85 bar. As the Reynolds number increases, the maximum lift coefficient gradually increases, while the pitch-up tendency vanishes. Lift-to-drag ratio also grows with Reynolds number.

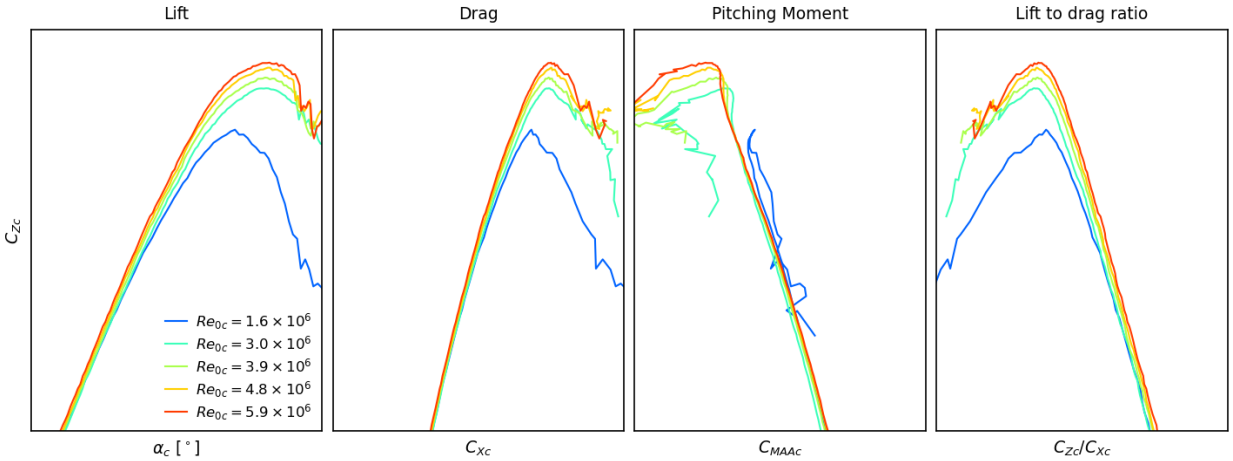

Figure 14: Longitudinal force coefficients of the LDG configuration, with tail planes, at Mach number M_{0c} = 0.20 and increasing Reynolds number Re_{0c} (runs 1309, 1496, 1476, 1441, 1387).

The wind tunnel pressurization enables varying the Mach number and the Reynolds number independently. Figure 15a displays the various flow conditions performed on this model configuration, each dot being a pitch-sweep run, colored by the maximum lift coefficient $C_{zc,\max}$ achieved. The light grey triangular shape is the operating envelope of the F1 wind tunnel. The same data are plotted in a different way in Figure 15b to show Reynolds number and Mach number effects separately. Dots are actual data from the wind tunnel runs, and lines are interpolation (based on Radial Basis Function) of all the runs shown in Figure 15a. As in most situations, the maximum lift coefficient increases with Reynolds number, for reasons detailed in [30] or [31]. The maximum lift coefficient did not reach a plateau in the range of Reynolds number tested, which is still far from full scale. However it evolves in an asymptotic way that helps in extrapolating to higher Reynolds numbers. Increasing the Mach number has a negligible effect up to Mach 0.2, but then causes a drop in maximum lift coefficient. This is attributed to the peak velocity on the leading edge of the slat reaching sonic conditions, see section V.F. Interestingly, very similar trends were reported for the Airbus A300 some 42 years ago [19].

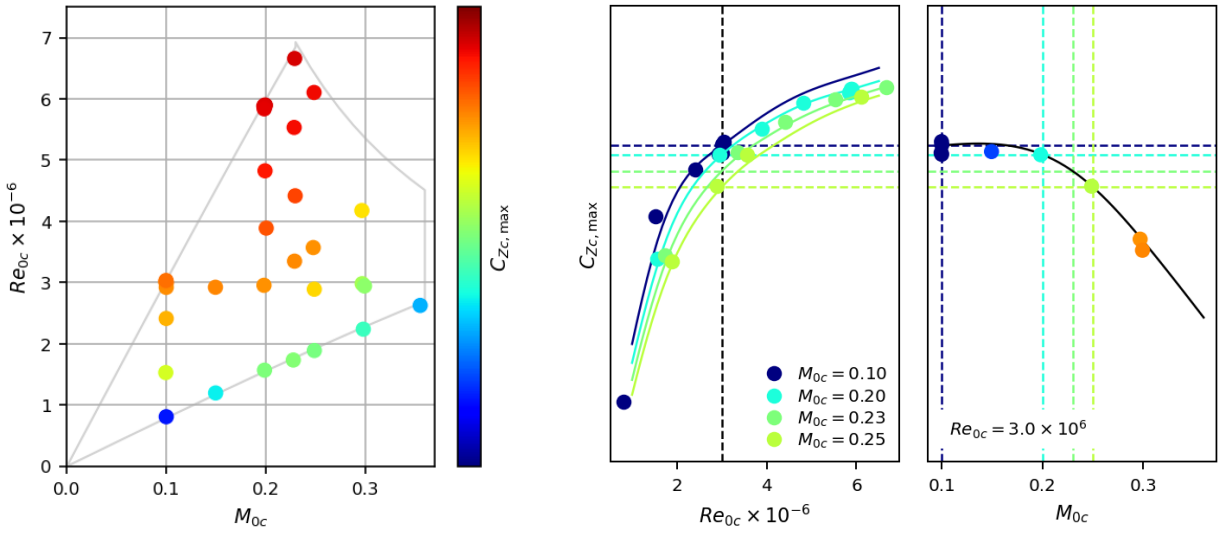

a. Combined effect in tunnel operating envelope **b. Segregated effect**

Figure 15: Effect of Mach and Reynolds numbers on maximum lift coefficient for the LDG configuration.

When performing runs by increasing tunnel velocity but under a constant total pressure, the competing effects of Reynolds and Mach numbers are involved simultaneously. In such a case, as illustrated in Figure 16, neither the Mach number nor the Reynolds number effect can be distinguished. Using only such results obtained in a constant pressure wind tunnel (e.g. atmospheric, i.e. curve p_{i0} = 1 bar in Figure 16), it would very difficult to propose any extrapolation to higher Reynolds numbers.

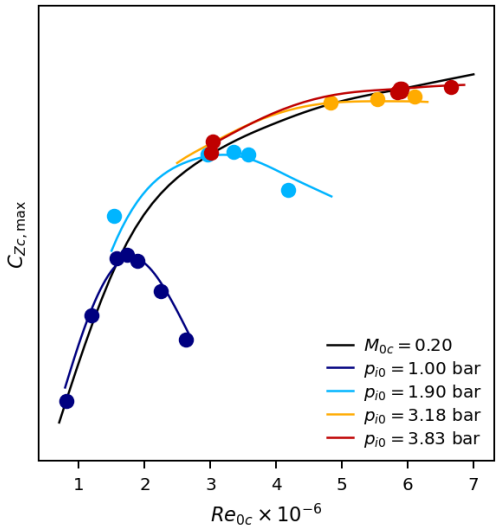

Figure 16: Evolution of maximum lift coefficient on LDG configuration, when increasing both Mach and Reynolds numbers at constant pressure (colored curves), or when increasing Reynolds number at constant Mach number (black curve).

2. Lateral characteristics

One way to identify the lateral behavior of the aircraft is to perform sweeps in sideslip angles, which is shown in Figure 17 for three different AoAs. The trend is as expected with symmetrical evolution in sideslip for the longitudinal forces (on the left), and asymmetrical for the lateral forces (on the right). Dots correspond to data taken from the AoA-sweep runs, when they "cross" the AoS-sweep runs.

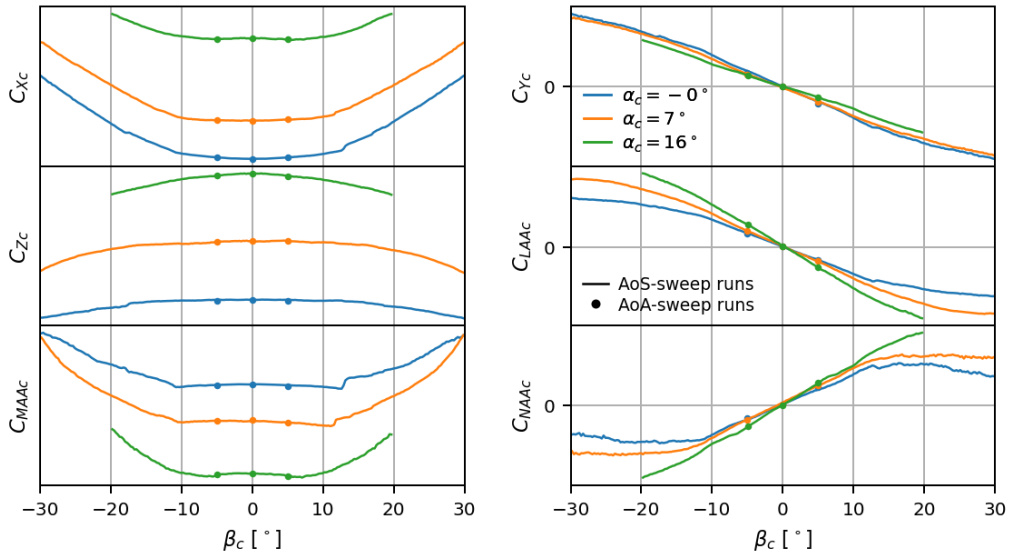

Figure 17: Force coefficients for AoS-sweep runs at different AoA on the LDG configuration at Mach number M_{0c} = 0.20 and Re_{0c} = 5.9 million (solid lines: AoS-sweep runs 1390, 1393, 1396; dots: AoA-sweep runs 1387, 1403, 1405).

Another way to look at lateral performance is to perform pitch-sweep runs at fixed sideslip angle, resulting in data presented in Figure 18. Focusing first on the run at β = 0°, this plot shows that the smooth maximum lift point is reached without any noticeable asymmetry in forces. This is no longer the case when progressing farther into stall: at about 2° beyond maximum lift point, the lift of the left wing drops first, causing negative rolling moment and positive yawing moment. Then, at about 3° beyond maximum lift point, the lift of the right wing drops as well, and brings lateral forces back to zero. At $\alpha_c \lesssim 15°$, small positive rolling and yawing moments exist. They are connected to the inner right wing generating less lift during this run, as already reported in section IV.D.

Looking now at the runs where a small AoS $\beta = \pm 5°$ was introduced, it is interesting to observe that the maximum lift coefficient is only slightly reduced and occurs about 1° earlier, compared with the runs at β = 0°.

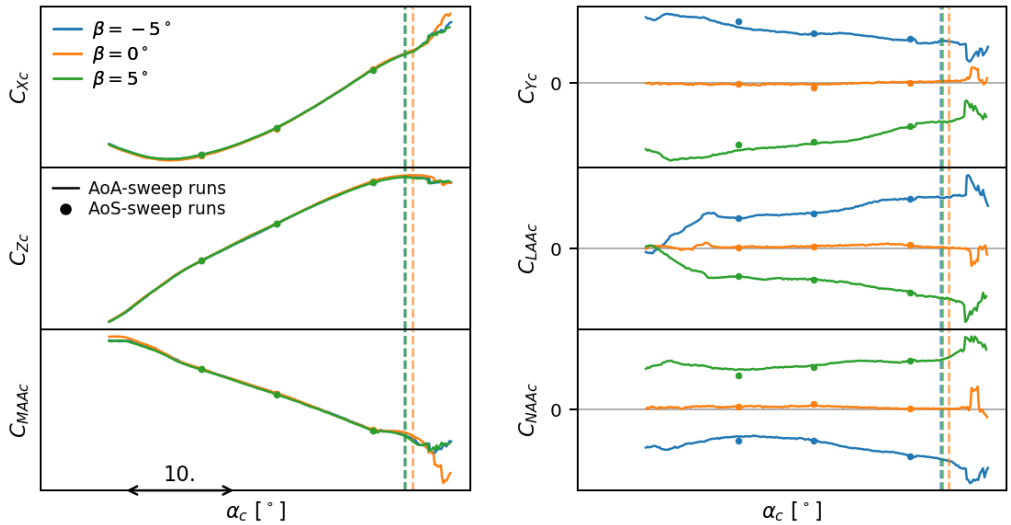

Figure 18: Force coefficients for pitch-sweep runs at different small AoS on the LDG configuration at Mach number M_{0c} = 0.20 and Re_{0c} = 5.9 million (solid lines: AoA-sweep runs 1387, 1403, 1405; dots: AoS-sweep runs 1390, 1393, 1396; dashed lines: α_c at maximum lift coefficient).

Data from Figure 18 can be used to evaluate the lateral force derivatives by performing a second-order finite difference calculation with respect to the AoS β, e.g.:

$$\left(\frac{\partial C_{NAc}}{\partial \beta}\right)_{\beta=0°} = \frac{C_{NAc}(\beta = 5°) - C_{NAc}(\beta = -5°)}{10°}$$

Another way to calculate lateral force derivatives is to examine the slope of the curves at $\beta = 0°$ in Figure 17, by performing a linear regression of force coefficients as a function of β in the range $-5° < \beta < +5°$. The result of these calculations is shown in Figure 19.

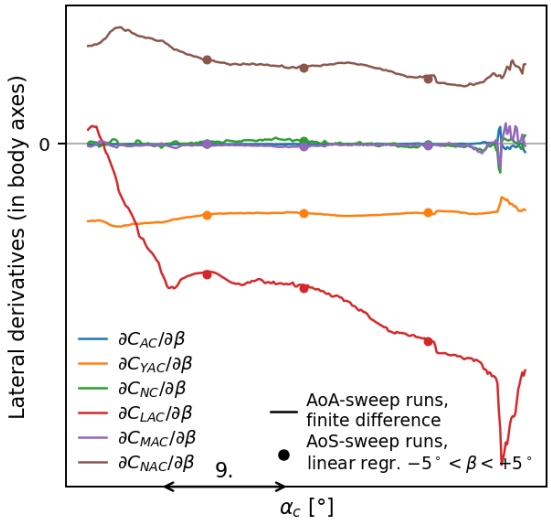

Figure 19: Lateral derivatives of force coefficients at Mach number M_{0c} = 0.20 and Re_{0c} = 5.9 million (solid lines: from finite difference across AoA-sweep runs 1403, 1405; dots: from linear regression of AoS-sweep runs 1390, 1393, 1396).

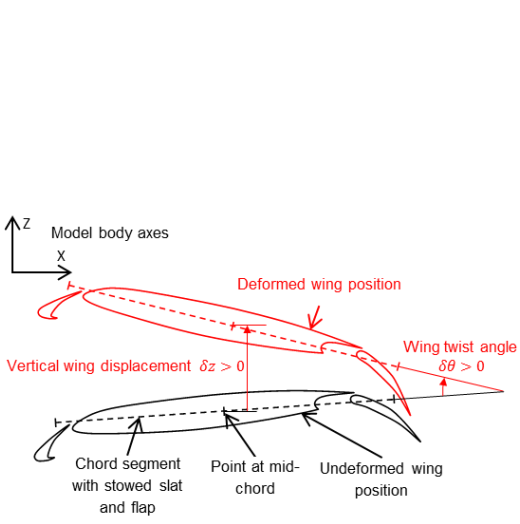

a. Schematic defining wing deformation parameters δz and $\delta\theta$.

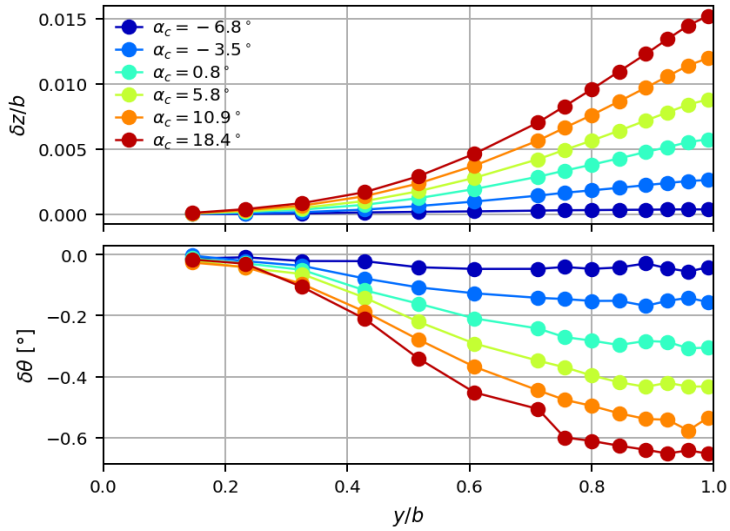

b. Measurements at Mach number M_{0c} = 0.20 and Re_{0c} = 5.9 million (run 1387).

Figure 20: Wing deformation measurement on LDG configuration.

3. Wing deformation

An example of wing deformation measurement is shown in Figure 20b, using nomenclature of Figure 20a. This run corresponds to a dynamic pressure of about 10 kPa, close to the highest one possible in F1, which is 14 kPa. The main aerodynamic effect of this deformation will stem from the wing twist $\delta\theta$, which reaches about −0.65° at wing tip, when lift is close to maximum. The corresponding wing tip deflection δz is 24 mm.

B. Landing configuration, without tail planes

Most previously published work about this configuration was carried out on a configuration without tail plane. For that reason, data without tails planes are presented in Figure 21, again at a Mach number of 0.20 and for increasing Reynolds number from 1.6 to 5.9 million. The pitch-up tendency at stall is better revealed in the pitching moment plot of this figure than it was in Figure 14, in which the stabilizing effect of the horizontal tail plane was dominating. Its dependency with Reynolds number is also better emphasized.

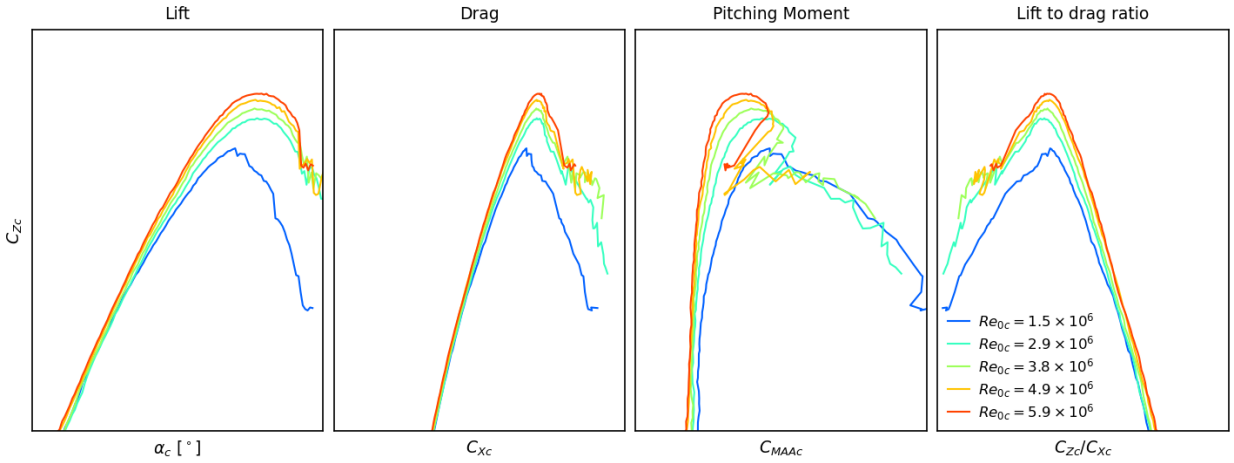

Figure 21: Longitudinal force coefficients of the LDG configuration, without tail planes, at Mach number M_{0c} = 0.20 and increasing Reynolds number Re_{0c} (runs 1943, 1901, 1887, 1871, 1814).

C. Take-off configuration, with tail planes

Similar plots and analyses can be carried out on the T/O configuration. The Figure 22 shows the longitudinal performance, at a Mach number of 0.20 and for increasing Reynolds number from 1.6 to 5.9 million. Like on the LDG configuration, at the lowest Reynolds number tested, maximum lift coefficient comes with a noticeable pitch-up tendency. This tendency reduces with increasing Reynolds number, but does not disappear until a Reynolds number of about 6 million is reached.

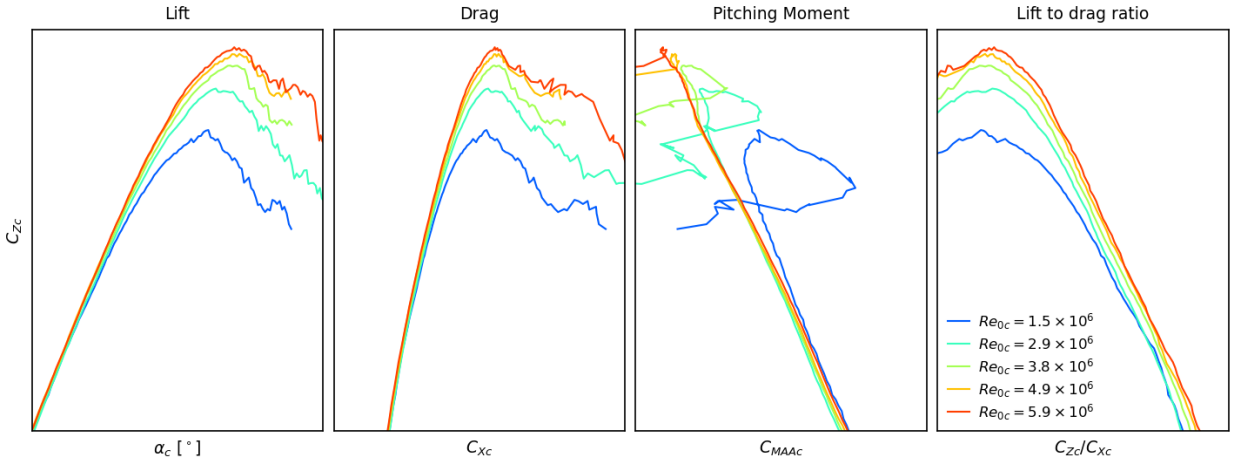

Figure 22: Longitudinal force coefficients of the T/O configuration at Mach number M_{0c} = 0.20 and increasing Reynolds number Re_{0c} (runs 2326, 2276, 2256, 2243, 1132).

Trends of the maximum lift coefficient with Reynolds and Mach number are shown in Figure 23, in a way that is identical to the Figure 15. Again, the maximum lift coefficient increases with Reynolds number, but decreases with Mach number, even with Mach number as low as 0.20.

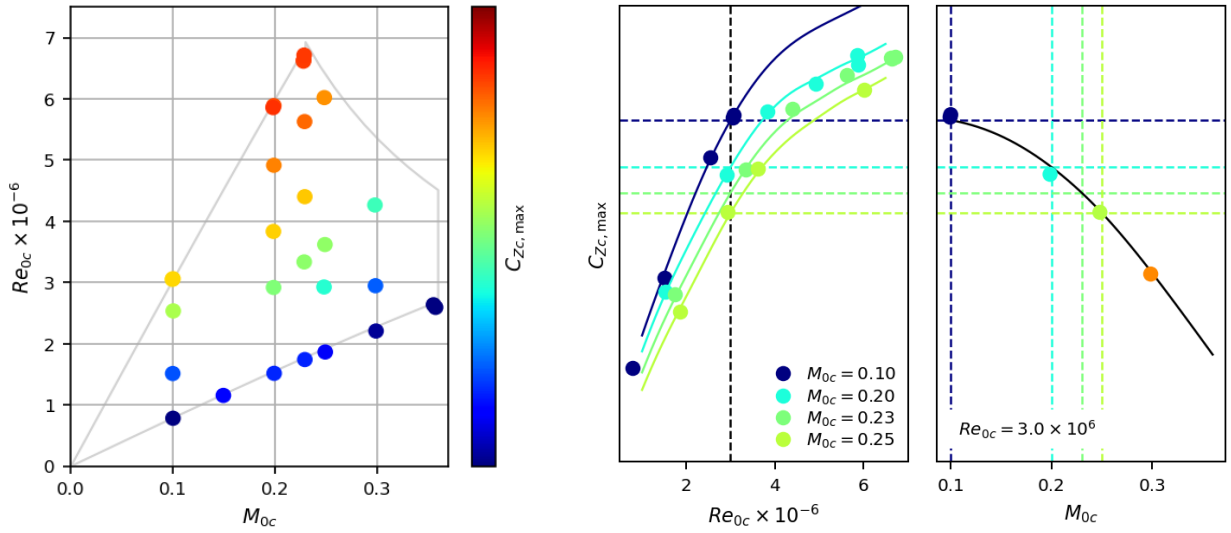

a. Combined effect in tunnel operating envelope **b. Segregated effect**

Figure 23: Effect of Mach and Reynolds numbers on maximum lift coefficient for the T/O configuration.

D. Build-up of the LDG configuration, with tail planes

Following suggestion from [18] section 4.8, several configurations of the model were tested, gradually building up the LDG configuration through intermediate configurations aiming at presenting increasingly complex flow physics. Results shown in Figure 24 start with the clean wing configuration, with tail planes. The clean wing results were obtained in a different test campaign, with the clean wing model (described in III.A.1) mounted on the same support and corrected in the same way as the present high-lift model campaign, as described in section IV. Data from the present campaign are then plotted, starting with the slat extended to their LDG position (curve "+ slat"). This configuration had no nacelle and a continuous slat, as described in section III.A.2. The flaps are then extended to their LDG position (curve "+ flap"). The nacelles and their pylon are then added to the previous configuration, but without the chine on the nacelle inner side (curve "+ nacelle"). Finally, the full LDG configuration is obtained by adding the chines on the nacelles.

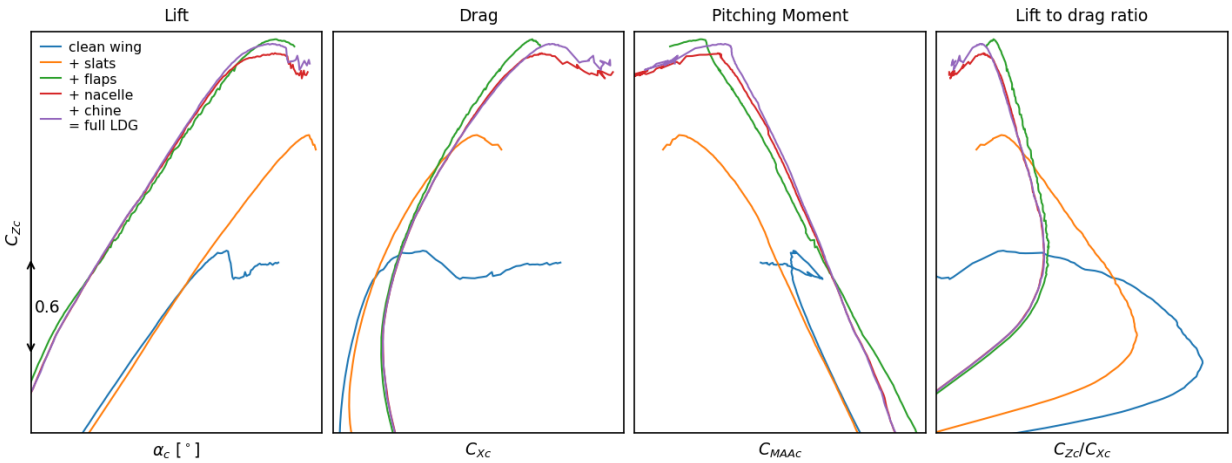

Figure 24: Longitudinal force coefficients for increasingly complex configurations at Mach number M_{0c} = 0.20 and Reynolds number Re_{0c} = 5.9 million (clean wing run 628, high-lift runs 1659, 1705, 1725, 1741).

E. Flap setting effect, without tail planes

After another suggestion from [18] section 4.7, two off-nominal deflections of the flaps were tested. The first one here called LDG-3 has a flap deflection angle reduced by 3° compared to the reference LDG configuration, and the other one called LDG+3 has a flap deflection angle increased by 3°. As a reminder, nominal flap deflection angles are 40° for the inboard flap and 37° for the outboard flap. These configurations were tested with no rear empennages, and at different Reynolds numbers. Results are reported in Figure 25. The more aggressive setting LDG+3 shows the largest maximum lift coefficient, at the expense of a larger drag at lower AoAs. A pitch-up is observed at stall for all configurations, but it arises earlier for the LDG−3 configuration. The ranking of the settings in terms of maximum lift coefficient and drag stays the same at low and high Reynolds number, which is not always the case.

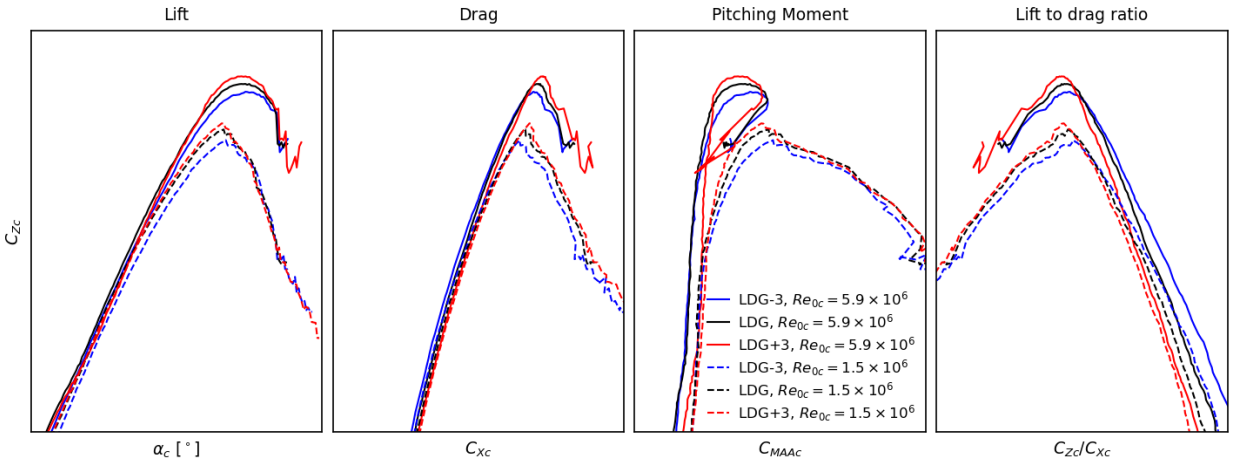

Figure 25: Flap deflection effect at Mach number M_{0c} = 0.20 and Reynolds number Re_{0c} = 1.6 million (dashed lines, runs 2113, 1943, 2211) and Re_{0c} = 5.9 million (solid lines, runs 2055, 1814, 2131).

F. Some flow physics considerations

Indications on local flow physics on the model are mostly provided by pressure measurements and by oil flow visualizations. They can be analyzed in a way similar to [33], but results will not be exposed in this paper, in the interest of the HPLW-5, see section VII. Nevertheless, to give an overview of available data, a possible utilization of pressure measurements on the model is presented in Figure 26.

In this figure, each dot comes from a pitch-sweep run, and presents the minimum pressure coefficient $C_{p,\min}$ observed on the model when it reaches maximum lift point $C_{zc,\max}$, as a function of Mach number. In some runs with the clean wing configuration, the lift never reaches a maximum but tends to level off. In that case, maximum lift point is replaced with the point where the drag suddenly increases and the lift slope strongly decreases. The Figure 26 helps in better understanding the roles of Reynolds and Mach numbers on maximum lift. At low Reynolds numbers (blue dots), the thick boundary layer cannot withstand a strong recompression so that the peak suction $C_{p,\min}$ is limited by the occurrence of flow separation, and therefore the maximum local Mach number remains small. In that case, flow separation is possibly influenced by laminar areas. As the Reynolds number Re_{0c} increases (yellow to red dots), higher peak velocity can be reached, typically with $C_{p,\min}$ of the order of −10 to −13, which corresponds to roughly 4 to 5 times the upstream velocity. But when the upstream Mach number M_{0c} increases above about 0.20 – 0.23, these high peak velocities locally become supersonic. Transonic phenomena, including the likely occurrence of shock waves and shock-induced flow separation, then start to negatively influence the maximum lift and pose limit values of $C_{p,\min}$. With the help of Figure 26, one can quickly understand how the flow physics at stall on this model can be different at M_{0c} = 0.20 ($C_{p,\min} \approx -13$ on the model, corresponding to a maximum local Mach number of 0.86) *vs* at M_{0c} = 0.30 ($C_{p,\min} \approx -9$ on the model, corresponding to a local maximum Mach number of 1.2). Similar trends and conclusions were exposed in [34], both for 2D airfoils and for 3D models, and they were successfully compared to flight test data. This figure also shows that this model, when tested at a total pressure p_{i0} of 1 to 2 bar, is unable to develop its full potential in terms on lift generation, as the peak velocity is limited by insufficient Reynolds number.

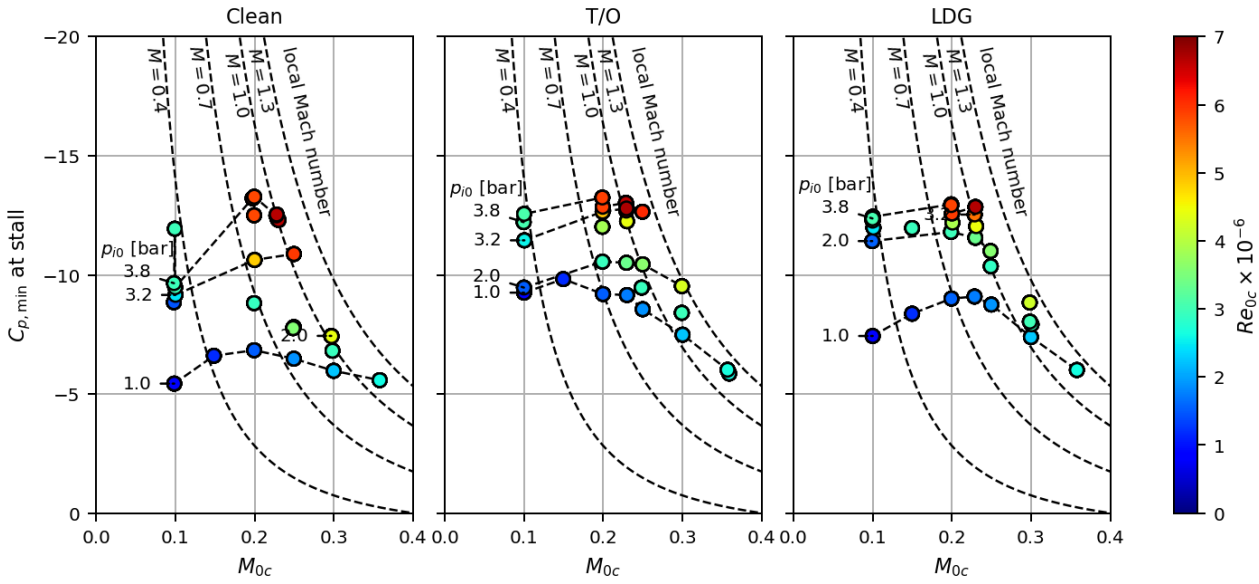

Figure 26: Minimum pressure coefficient observed across all taps of the model, at AoA corresponding to maximum lift point, as a function of Mach and Reynolds numbers, for clean, T/O and LDG configurations; straight dashed lines indicate the total pressure p_{i0} of the different runs, and curved dash lines indicate the local Mach number corresponding to the pressure coefficient.

Finally, an example of oil flow visualization is provided in Figure 27. It exhibits separated flow region on the outboard wing, with triangular shape, downstream of each slat bracket, as was already the case in [10]. High resolution pictures and flow conditions will be revealed later.

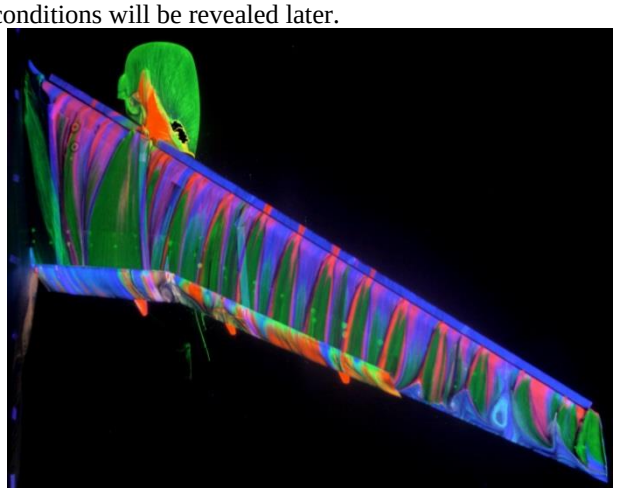

Figure 27: Oil flow visualization on the suction side of right wing (aircraft configuration and flow conditions to be revealed latter, see section VII).

VI. Perspectives for future tests

As explained in introduction, this LRM-HL model is intended to be used on multiple occasions in the future. At the end of 2022, an additional test campaign, not reported in this paper, was already carried out, using Particle Image Velocimetry (PIV) measurements, in several areas of the model wake and near the wing surface, as can be seen in Figure 28.

A test campaign featuring acoustic measurement of airframe noise, using an acoustic antenna positioned on the wind tunnel floor, is planned in 2023. Investigations of ground effect will also be carried out shortly.

Plans for the future years include wing measurements using Pressure Sensitive Paint, mounting on a different wind-tunnel setup using a floor balance, and icing effect.

Figure 28: PIV planes carried out on LDG configuration.

VII. Data sharing policy

The documentation, Computer Aided Design (CAD) shapes and dataset collected during this test campaign is planned to be shared at different occasions, and with different partners. Selected data will be made publicly and freely available under CC-BY-NC-ND license.

A tentative timeline for public data release in indicated below:

- January 2023 at AIAA Scitech (present paper): main characteristics of the wind tunnel experiment and content of the dataset;
- March 2023: model geometry and wing deformation;
- June 2024 at HPLW-5: dataset for the official test cases of the HLPW-5.

This timeline was chosen to be compatible with the HLPW-5 agenda. Indeed, this experimental database is a candidate for one of the test cases of the workshop. Limited data release was decided, in order to have simulations of this configuration carried out blindly before the workshop. The official test cases of the HLPW-5 should be announced around March 2023.

Beyond this public release, possible agreements and collaborations with selected partners are possible.

VIII. Conclusion

The main features and outcomes of the wind tunnel testing of the LRM-HL full-span model in the ONERA F1 pressurized low-speed wind tunnel have been presented. A large amount of data has already been collected during this first test covering large variations in model configurations, AoA, AoS, Mach and Reynolds numbers, and including force, pressure, wing deformation, and flow visualization data. The main elements of the test methodology were provided to better appreciate the quality of the database in terms of uncertainty, repeatability, and wall and support corrections.

The available dataset should be very relevant as a CFD validation test case for high-lift configurations in the future, possibly in the HLPW-5. More generally, it should be useful for the scientific community dealing with high-lift flow.

A short analysis of this database was provided, which evidenced the importance of separating Reynolds number effects from Mach number effects. Indeed, both were shown to have significant effects on performance of high-lift aircraft configuration, through very different physical phenomena. Separating them is necessary to be able to extrapolate wind tunnel results to actual flight conditions. Such an analysis is enabled by the pressurization capability of a facility like the ONERA F1 wind-tunnel.

Acknowledgements

This work was funded by ONERA's research budget as part of the continual improvement of its wind-tunnel testing services. Some parts of the model were founded by a loan with the European Investment Bank. The authors

would like to thank the teams in the design office, in the model workshop and in the wind tunnel for their contribution.

References

[1] Slotnick, J., Khodadoust, A., Alonso, J., Darmofal, D., Gropp, W., Lurie, E., and Mavriplis, D., "CFD Vision 2030 Study: A Path to Revolutionary Computational Aerosciences, NASA/CR-2014-218178, March 2014. https://ntrs.nasa.gov/archive/nasa/casi.ntrs.nasa.gov/20140003093.pdf.

[2] Rumsey, C. L., Slotnick, J. P., and Sclafani, A. J., "Overview and Summary of the Third AIAA High Lift Prediction Workshop," AIAA Paper 2018-1258, January 2018. doi:10.2514/6.2018-1258

[3] AIAA High Lift Prediction Workshop: https://hiliftpw.larc.nasa.gov/, retrieved 31 May, 2022.

[4] Clark, A. M., Slotnick, J. P., Taylor, N., and Rumsey, C. L., "Requirements and Challenges for CFD Validation using the High-Lift Common Research Model," AIAA Paper 2020-2772, June 2020. doi: 10.2514/6.2020-2772

[5] Lacy, D. S., and Sclafani, A. J., "Development of the high lift common research model (HL-CRM): A representative high lift configuration for transonic transports," AIAA Paper 2016-0308, January 2016. doi:10.2514/6.2016-0308

[6] Rivers, M. B., "NASA Common Research Model: A History and Future Plans," AIAA Paper 2019-3725, June 2019. doi:10.2514/6.2019-3725

[7] Vassberg, J.C., DeHaan, M.A., Rivers, S.M., Wahls, R.A., "Development of a Common Research Model for Applied CFD Validation Studies," AIAA Paper 2008-6919, August 2008. doi:10.2514/6.2008-6919

[8] Lin, J.C., Melton, L. P., Viken, S. A., Andino, M. Y., Koklu, M., Hannon, J. A., and Vatsa, V.N., "High Lift Common Research Model for Wind Tunnel Testing: An Active Flow Control Perspective," AIAA Paper 2017-0319, January 2017. doi:10.2514/6.2017-0319

[9] Lin, J.C., Melton, L. P., Hannon, J. A., Andino, M. Y., Koklu, M., Paschal, K. B., and Vatsa, V. N., "Wind Tunnel Testing of Active Flow Control on High Lift Common Research Model," AIAA Paper 2019-3723, June 2019. doi:10.2514/6.2019-3723

[10] Evans, A., Lacy, D., Smith, I., and Rivers, M., "Test Summary of the NASA Semi-Span High-Lift Common Research Model at the QinetiQ 5-Metre Low-Speed Wind Tunnel," AIAA paper 2020-2770, June 2020. doi:10.2514/6.2020-2770

[11] Lockard, D.P., Turner, T.L., Bahr, C.J., and Hutcheson, F.V., "Overview of Aeroacoustic Testing of the High-Lift Common Research Model," AIAA Paper 2021-2113, August 2021. doi:10.2514/6.2021-2113

[12] Goc, K.A., Moin, P., and Bose, S.T., "Large Eddy Simulation of the NASA High-Lift Common Research Model, AIAA Paper 2022-1556, January 2022. doi:10.2514/6.2022-1556

[13] Lacy, D. S., and Clark, A. M., "Definition of Initial Landing and Takeoff Reference Configurations for the High Lift Common Research Model (CRM-HL)," AIAA Paper 2020-2771, June 2020. doi:10.2514/6.2020-2771

[14] Cartieri, A., Hue, D., Chanzy, Q., and Atinault, O., "Experimental Investigations on Common Research Model at ONERA-S1MA–Drag Prediction Workshop Numerical Results," *Journal of Aircraft*, Vol. 55, No. 4, July 2018. doi: 10.2514/1.C034414

[15] Cartieri, A., Hue, D., "Using RANS computations to calculate support interference effects on the Common Research Model," Advanced Wind Tunnel Boundary Simulation, MP-AVT-284, NATO, 2018. doi: 10.14339/STO-TR-AVT-284

[16] Cartieri, A., "Experimental investigations on the Common Research Model at ONERA-S2MA," Paper AIAA 2020-0779, January 2020. doi: 10.2514/6.2020-0779

[17] Chyczewski, T.S., Lofthouse, A.J., Gea, L.-M., Cartieri, A., and Hiller, B.R., "Summary of the First AIAA Stability and Control Prediction Workshop," Paper AIAA 2022-1680, January 2022. doi: 10.2514/6.2022-1680

[18] Clark, A.M., Slotnick, J.P., Taylor, N., and Rumsey, C.L., "Requirements and Challenges for CFD Validation within the High-Lift Common Research Model Ecosystem," AIAA Paper 2020-2772, June 2020. doi:10.2514/6.2020-2772

[19] Carrara, J.-M., and Masson, A., "Three Years of Operation of the ONERA Pressurized Subsonic Wind Tunnel," *12th Congress of the International Council of the Aeronautical Sciences*, ICAS, Bonn, October 1980, pp. 778–792, https://hal.archives-ouvertes.fr/hal-03224252.

[20] Woodward, D.S., François, G., Taylor, N.J., "The Aerodynamic and Structural Design of the DRA 5-Metre and ONERA F1 Low-Speed Pressurised Wind Tunnels," *Aerodynamics of Wind Tunnel Circuits and their Components*, AGARD-CP-585, 1997.

[21] Hoelmer, W., Younghans, J. L., and Raynal, J.-C., "Effect of Reynolds Number on Upper Cowl Flow Separation," Journal of Aircraft, Vol. 24, No. 3, 1987, pp. 161–169. doi:10.2514/3.45411
[22] Mouton, S., "Numerical Simulation of the Flow in the ONERA F1 Wind Tunnel," to be published in *Journal of Aircraft*. doi: 10.2514/1.C036880
[23] Vaucheret, X., "Recent Calculation Progress on Wall Interferences in Industrial Wind Tunnels," *La Recherche Aérospatiale*, No. 3, pp 45-47, 1988.
[24] Hantrais-Gervois, J.L., and Piat, J.F., "A Methodology to Derive Wind Tunnel Wall Corrections from RANS Simulations," *Advanced Wind Tunnel Boundary Simulation*, STO-MP-AVT-284, NATO/STO, March 2018. doi:10.14339/STO-TR-AVT-284
[25] Ewald, B.F.R. (Ed.), *Wind Tunnel Wall Corrections*, AGARD-AG-336, 1998.
[26] Quémard, C., and Earnshaw, P.B., "Comparison of the results of tests on A300 aircraft in the RAE 5 metre and the ONERA F1 wind tunnels," *Aerodynamic Data Accuracy and Quality: Requirements and Capabilities in Wind Tunnel Testing*, AGARD-CP-429, July 1988.
[27] Lee, S., Broeren, A., Woodard, B.S., Lum, C.W., and Smith, T.G., "Comparison of Iced Aerodynamic Measurements on a Swept Wing from Two Wind Tunnels," AIAA Paper 2018-3493, June 2018. doi:10.2514/6.2018-3493
[28] Saiz, M., and Quémard, C., "Airbus A310 Essais dans la soufflerie F1 de l'ONERA Comparaison vol-soufflerie," *Wind Tunnels and Testing Techniques*, AGARD-CP-348, February 1984.
[29] S. Mouton, "Numerical investigations of model support interference in subsonic and transonic wind tunnels," *8th ONERA-DLR Aerospace Symposium*, October 17-19, 2007, Göttingen, Germany. https://hal.archives-ouvertes.fr/hal-03017003v1
[30] Smith, A.M.O., "High-Lift Aerodynamics," *Journal of Aircraft*, Vol. 12, No. 6, June 1975. doi:10.2514/3.59830
[31] Woodward, D.S., Hardy, B. C., and Ashill, P. R., "Some Types of Scale Effect in Low-Speed, High-Lift Flows," ICAS Paper 4.9.3, Jerusalem, 1988.
[32] Bousquet, J. M., Lyonnet, M., and Mignosi, A., "New Measurement Techniques in the Onera Large Wind-Tunnels," 25th Congress of the International Council of the Aeronautical Sciences,Vol. 3, ICAS, Bonn, 2006, pp. 1652–1660. https://hal.archives-ouvertes.fr/hal-03224281
[33] Rudnik, R., "Stall Behaviour of the EUROLIFT High Lift Configurations," AIAA Paper 2008-836, January 2008. doi:10.2514/6.2008-836
[34] Thibert, J.J., "The GARTEUR High Lift Research Programme", *High-Lift System Aerodynamics*, AGARD-CP-515, September 1993.